



Structural, Morphological and Interfacial Investigation of $\text{H}_2\text{V}_3\text{O}_8$ upon Mg^{2+} Intercalation

Yuri Surace,^{*[a]} Martina Romio,^[a] Marco Amores,^[a] Raad Hamid,^[a] Damian Cupid,^[a] Markus Sauer,^[b] Annette Foelske,^[b] and Marcus Jahn^[a]

Magnesium-ion batteries (MIBs) are a promising alternative to lithium-ion batteries due to their higher theoretical energy densities and lower cost. However, fundamental limitations such as the sluggish diffusion of Mg^{2+} ions into cathode materials have hindered their practical implementation. In this work, the structural, morphological and interfacial changes of $\text{H}_2\text{V}_3\text{O}_8$, a promising cathode material for MIBs, are elucidated upon Mg^{2+} intercalation in TFSI-based electrolytes. Post-mortem analysis revealed a shrinkage of the interlayer distance, an increase in cell volume, and a decrease of the surface $\text{V}^{5+}/\text{V}^{4+}$ ratio during discharge. These changes were only partially

reversible upon subsequent charge due to Mg trapping. A cathode electrolyte interphase (CEI) formed mainly of TFSI^- -anions, its decomposition products, and MgF_2 was detected on the surface of $\text{H}_2\text{V}_3\text{O}_8$. The CEI thickness and chemical composition vary upon charge and discharge as well as during prolonged cycling, and its presence correlates with the additional capacity recorded during discharge. Our study aims to contribute to a better understanding of Mg^{2+} intercalation and cathode-electrolyte interaction in high voltage cathode materials for MIBs.

Introduction

For the last three decades, lithium-ion batteries (LIBs) have been the dominant power source for portable electronic devices. However, fast-growing applications such as electric vehicles and large-scale stationary energy storage systems require rechargeable batteries with improved specific energy, energy density, and power properties.^[1] As the use of LIBs becomes more widespread, many concerns have been raised regarding their safety and environmental sustainability. Specifically, LIBs are known to have safety issues due to Li dendrite formation during the charge step,^[2] which can lead to short-circuiting of the battery and thermal runaway. Furthermore, the environmental and economic sustainability of LIBs needs to be addressed, as state-of-the-art LIBs use transition-metal oxide cathodes containing critical raw materials such as cobalt, and electrode production is performed using toxic solvents such as N-methyl pyrrolidone.^[3,4] Therefore, a worldwide effort is underway to develop “next-generation” batteries based on new

chemistries with better electrochemical performance, safety, lower cost and more environmentally friendly properties than LIBs.^[5–8]

Magnesium-ion batteries (MIBs) have received considerable attention during the last few years as an alternative battery chemistry to LIBs due to the intrinsic advantages of Mg over Li when the pure metals are used as the anode. Mg has a significantly larger volumetric capacity (3832 mAh cm^{-3} vs. 2061 mAh cm^{-3} for Li^[9]), high natural abundance,^[10] lower cost,^[11] and relatively low standard redox potential (-2.37 V vs. standard hydrogen electrode^[9]). Theoretical calculations have also shown that Mg metal exhibits non-dendritic electrodeposition,^[12] and this was experimentally demonstrated at practical current densities of 2 mA cm^{-2} ,^[13] therefore MIBs are expected to be safer than LIBs. Furthermore, since Mg^{2+} is a divalent cation, for the same amount of moles of ions stored in a host material, the specific capacity of Mg^{2+} is double than that of monovalent cations such as Li^+ . Thanks to these key advantages, MIBs can theoretically achieve higher energy densities at a lower cost than LIBs^[5] making MIBs a very attractive battery technology.

However, one of the fundamental limitations of MIBs is the slow Mg^{2+} ion solid state diffusion into the cathode active material's lattice during intercalation. This is generally attributed to the high charge/radius ratio of the Mg^{2+} ion, which results in large activation energies for migration due to the strong electrostatic interactions with the negatively charged ions in the cathode lattice.^[14,15] As a consequence, cathode materials for MIBs usually show low practical specific capacities, high overpotentials and poor rate capability.^[16–18] Therefore, finding a host cathode material which possesses good electrochemical performance as well as a high voltage and capacity is the key to MIBs' realization.

[a] Dr. Y. Surace, Dr. M. Romio, Dr. M. Amores, R. Hamid, Dr. D. Cupid, Dr. M. Jahn
Battery Technologies, Center for Low-emission Transport,
AIT Austrian Institute of Technology GmbH
Giefinggasse 4, 1210 Vienna (Austria)
E-mail: yuri.surace@ait.ac.at

[b] Dr. M. Sauer, Dr. A. Foelske
Analytical Instrumentation Center,
Technische Universität Wien
Lehargasse 6, Objekt 10, 1060, Vienna (Austria)

Supporting information for this article is available on the WWW under <https://doi.org/10.1002/batt.202200555>

© 2023 The Authors. *Batteries & Supercaps* published by Wiley-VCH GmbH. This is an open access article under the terms of the Creative Commons Attribution License, which permits use, distribution and reproduction in any medium, provided the original work is properly cited.

Due to their success in LIBs,^[19,20] vanadium-based oxides (vanadates) have been considered a promising class of cathodes for MIBs due to their large interlayer distance (up to 11 Å), high working potentials vs. Mg²⁺/Mg (\approx 2.0–2.5 V), high theoretical specific capacity (150–200 mAh g⁻¹) derived from the possibility of vanadium to occupy multiple oxidation states (i.e. V⁵⁺/V⁴⁺ and V⁴⁺/V³⁺) and low cost.^[11,21] Within this class, H₂V₃O₈ (V₃O₇·H₂O), in short HVO, is a very promising member. Indeed, HVO has already attracted attention as a host cathode for monovalent (Li⁺^[22–24] and Na⁺^[25,26]) and divalent ions (Zn²⁺),^[27] and only very recently, it has been shown to be able to intercalate Mg²⁺ ions.^[28,29] In fact, HVO's theoretical specific capacity of 190 mAh g⁻¹ or 380 mAh g⁻¹, per 1 equiv. or 2 equiv. of intercalated Mg²⁺ ions per formula unit, respectively, is among the highest for cathode materials. Due to its layered structure, which consists of V₃O₈ layers stacked along the α -axis, providing vacant sites in the interlayer space, HVO can intercalate single and multi-valent cations.^[30–32] Structural water molecules are directly bonded to the vanadium atom of a VO₅ polyhedron and connect two neighboring V₃O₈ layers by hydrogen bonds. The presence of structural water provides an elastic buffer space between the V₃O₈ layers,^[33] hence facilitating the non-destructive (de-) intercalation of cations. In addition, HVO can be synthesized with tailored nanostructure morphologies with high surface-area to volume ratios, thereby increasing the contact areas between the electroactive material and electrolyte as well as decreasing the total diffusion lengths. The layered structure and the morphology serve to increase the number of cations which can diffuse into the host structure as well as the power/rate capabilities of the resulting cell.

Despite these promising characteristics, the intercalation of Mg²⁺ cations into HVO has only been demonstrated in three recent works. Tang et al.^[28] reported a surprisingly high specific capacity of around 300 mAh g⁻¹ at room temperature using a 0.5 M Mg(ClO₄)₂ in acetonitrile (ACN) electrolyte. Rastgooy-Deylamy et al.^[29] tested HVO in the same electrolyte and showed that the very high specific capacity in Ref. [28] was due to the presence of water in the electrolyte, which is known to enhance Mg²⁺ intercalation.^[34] However, water is incompatible with Mg metal anodes due to the formation of insoluble, MgO/Mg(OH)₂ layers at the metal/electrolyte interface, which passivate the Mg anode and inhibit the electrodeposition of Mg due to their low Mg²⁺ ionic conductivity.^[35,36] Therefore, although electrolytes containing small concentrations of water can improve the intercalation of Mg²⁺ ions into the cathode host structures, they cannot be combined with the metallic Mg anodes. Indeed, once a water-free electrolyte was used, a significantly lower specific capacity of only about 80 mAh g⁻¹ was obtained at room temperature.^[29] Very recently Söllinger et al.^[37] reported the electrochemical performance and operando XRD of HVO in Mg(ClO₄)₂-based electrolytes with different amounts of water. It was demonstrated that the capacity of the materials increases with increasing amount of water in the electrolyte.

To the best of our knowledge, the intercalation of Mg²⁺ into HVO using an electrolyte other than Mg(ClO₄)₂ in ACN has never been reported. Furthermore, a systematic investigation

of the changes in the bulk and surface properties of HVO due to Mg²⁺ intercalation upon long-term cycling has not been performed. In our study, the changes in crystal structure, morphology and chemistry of the electrode/electrolyte interphase occurring in HVO upon Mg²⁺ intercalation using a TFSI-based electrolyte are investigated. Post-mortem analysis, combining bulk and surface characterization, was carried out on pristine HVO electrodes, as well as upon charge and discharge at selected cycle numbers. It is demonstrated that Mg²⁺ ions can be intercalated into HVO in TFSI-based electrolytes, thereby changing the lattice parameters of HVO. Evidence of Mg trapping as well as of a cathode electrolyte interphase (CEI) forming on the HVO surface as a result of electrolyte decomposition is shown, and these observations are correlated with the electrochemical performance.

Results and Discussion

The electrochemical performance of HVO was investigated in 0.1 M Mg(TFSI)₂ electrolyte at room temperature. Before starting the measurements, the working electrodes were kept at OCV for 6 h to observe the change in potential as a function of time. The OCV of HVO just after assembling the cell was approximately 0.37 V vs. AC (2.97 V vs. Mg²⁺/Mg) (Figure S1). The OCV decreases over time to attain a value of 0.08 V vs. AC (2.68 V vs. Mg²⁺/Mg) after 6 h. This decrease in OCV may be attributed to the distribution of the electrolyte and the equilibration of the cell components in contact with electrolyte (HVO and AC). The change in the discharge and charge potential profiles over 50 cycles is shown in Figure 1(a) and selected cycles are shown in Figure S2. In the 1st discharge, HVO shows a low specific capacity of 40 mAh g⁻¹ and a sloping potential profile, which can indicate the occurrence of a single-phase intercalation mechanism.^[29] During the 1st charge, a distinct change in slope of the charge curve is observed at around 0.5 V vs. AC (3.1 V vs. Mg²⁺/Mg), which is in agreement with the oxidation peak shown in the cyclic voltammetry (Figure S3). The large differences in the potentials between the 1st discharge and 1st charge (Figure S2), also known as overpotential, may be attributed to the sluggish kinetics of Mg²⁺ insertion into (discharge) and extraction from (charge) the HVO cathode active material in the first cycle.

As the cycling proceeds, several phenomena are observed to take place. Firstly, the overpotential on charge increases, and a defined plateau forms at 0.65 V vs. AC. Simultaneously, the specific capacities of the discharge and charge reactions increase. Following this trend in the first 10 cycles, the overpotential abruptly decreases, thereby leading to a rapid increase in specific capacity up to 220 mAh g⁻¹ and 130 mAh g⁻¹ at the end of the 25th discharge and charge steps, respectively. At the 50th cycle, the discharge capacity decreases from 220 mAh g⁻¹ at the 25th cycle to 180 mAh g⁻¹, whereas the charge cycle remains relatively constant at 130 mAh g⁻¹.

An increase in specific capacity during cycling is commonly observed in Mg-ion literature.^[34,38–45] Although such phenomenon is still poorly understood, it is generally related to: 1)

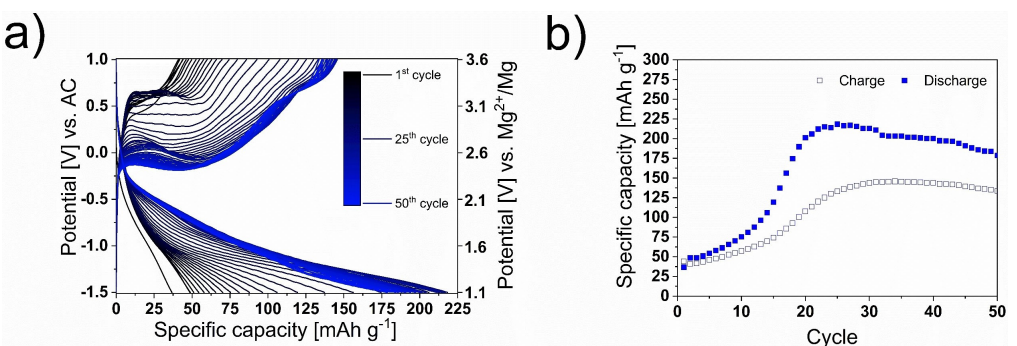


Figure 1. a) Potential profile of HVO electrodes for cycle 1 to 50 in 0.1 M Mg(TFSI)₂ in ACN at 10 mA g⁻¹. b) Specific capacity vs. cycle number.

structural deformation with gradual changes in the crystal structure of the host lattice, enabling it to more effectively accommodate the de-/intercalation of Mg²⁺, 2) the occurrence of phase transitions, 3) a gradual wetting of the electrode with the electrolyte, 4) a change in the electronic conductivity of the cathode, and 5) interfacial stabilization. Specifically, it is not uncommon to observe an increase of capacity in the initial cycles for vanadates.^[34,39,41,43–45]

However, the considerable difference between the specific charge and discharge capacities is unusual and needs to be further investigated. In addition, the high capacities obtained in

the TFSI-based electrolyte might also reflect changes in the material, which need to be elucidated.

Therefore, post-mortem investigations of the HVO electrodes were carried out after charge and discharge at selected cycle numbers to gain insights into the changes in the crystal structure, morphology and chemistry of the electrode/electrolyte interphase upon Mg²⁺ de-/intercalation. The analyzed electrodes are listed in Table 1.

The measured XRD patterns of the electrodes are shown in Figure 2. The diffractogram of the pristine electrode confirms that HVO which was synthesized has an orthorhombic crystal structure (ICSD: 80572, space group *Pnma*, $a = 16.930 \text{ \AA}$, $b = 3.644 \text{ \AA}$, and $c = 9.359 \text{ \AA}$ ^[31]) with the main (200) reflection at $2\theta = 10.3^\circ$. The measured patterns of HVO-OCV, HVO-1D and HVO-1C do not show any noticeable peak shifts, which indicate only very minor changes in the crystal structure at these states. Instead, the measured XRD patterns of the HVO-25D and HVO-50D electrodes, which are in the discharge state, show considerable changes of the major reflections. The (200) peak shifts to higher 2θ angles, indicating a reduction in the interlayer distance upon Mg²⁺ intercalation,^[29,46] and overlaps with the (101) reflection. The (201) and (302) reflections almost disappear, which may be due to a loss of symmetry in the crystal lattice due to Mg²⁺ intercalation. Furthermore, the (301) and (502) peaks shift to higher 2θ angles and exhibit lower intensities while becoming broader.

Table 1. Summary of the analyzed electrodes.

Electrode name	Description of the cycling conditions
HVO-pristine	No cycling, Fresh electrode
HVO-OCV	OCV for 6 h
HVO-1D	OCV for 6 h, discharge to -1.5 V vs. AC (1 st discharge)
HVO-1C	OCV for 6 h, discharge to -1.5 V vs. AC and then charge to 1.0 V vs. AC (1 st charge)
HVO-25D	OCV for 6 h, discharge to -1.5 V vs. AC at the 25 th cycle (25 th discharge)
HVO-25C	OCV for 6 h, discharge to -1.5 V vs. AC and then charge to 1.0 V vs. AC at the 25 th cycle (25 th charge)
HVO-50D	OCV for 6 h, discharge to -1.5 V vs. AC at the 50 th cycle (50 th discharge)
HVO-50C	OCV for 6 h, discharge to -1.5 V vs. AC and then charge to 1.0 V vs. AC at the 50 th cycle (50 th charge)

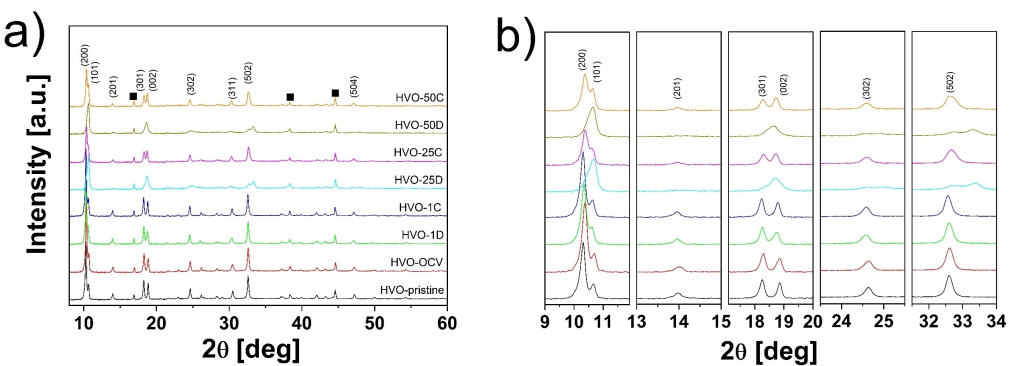


Figure 2. a) XRD patterns of HVO electrodes at specific cycle numbers. b) Zoomed-in sections of the XRD patterns at selected angle ranges. Black squares indicate reflections of the Al current collector.

The measured XRD patterns of the HVO-25C and HVO-50C electrodes (charged state) show that the shift of the (200), (301) and (502) peaks is reversible, but only partially, since the reflections move to lower 2θ angles but do not retain their initial positions. In addition, the peaks are broader, indicating a possible loss of crystallinity over cycling. Interestingly, the (201) and especially the (302) peaks reappear upon charge.

In order to gain more quantitative information on the changes in the crystal structure upon Mg^{2+} intercalation, Lebail fitting was performed on all XRD patterns (Figures S4–S11). The evolution of the lattice parameters and unit cell volume upon cycling is shown in Figure 3. The data are summarized in Table S1, whereas Table S2 reports the relative percentage changes. The lattice parameters of HVO-pristine are $a = 16.8429(6)$ Å, $b = 3.6280(4)$ Å, $c = 9.3110(3)$ Å and the unit cell has a volume of $568.96(7)$ Å³. The lattice parameters of the HVO phase in the HVO-OCV electrode undergo very small changes, with the most noticeable increase observed for the volume which increases by +0.6%.

In comparison to HVO-pristine, the a , b and c lattice parameters of the HVO active material in the HVO-1D electrode change by -0.18%, +0.64%, +0.71%, respectively, and the volume increases by +1.17%. Upon 1st charge, the a , b and c lattice parameters as well as the cell volume almost retain their initial values, showing a difference of just below +0.1% for the three axes and +0.24% for the cell volume. The lattice parameters of the HVO active material in the HVO-25D and HVO-50D undergo significant changes, in agreement with Figure 2 and the qualitative analysis reported above. For both samples, the a axis decreases by $\approx -0.5\%$, whereas the b axis increases up to +5% and the c axis increases between +1 and +3%. The volume increases by more than +6%. Such a large increase in the unit cell volume can be related to the considerable amount of Mg^{2+} ions intercalated into HVO structure in correlation with the high specific discharge capacities of 220 mAh g⁻¹ and 180 mAh g⁻¹ recorded for the 25th and 50th discharge, respectively.

An analysis of the percentage changes upon charge, either after the 25th or 50th cycle, reveals that the lattice parameters and unit cell volume of HVO do not attain the values of the

pristine sample. Indeed, HVO-25C and HVO-50C show a difference with HVO-pristine of up to -0.3%, +3%, +1% and +4% for the a , b , c axes and cell volume, respectively. This difference may be related to a certain amount of Mg^{2+} ions being trapped in the crystal structure of HVO or to irreversible structural changes, i.e., due to the mechanical stress that the crystal structure undergoes upon magnesiation, rendering it unable to return to its initial state upon demagnesiation within the voltage window studied.

Generally, upon discharge, the a axis decreases, while the b and c axes increase, leading to an increase in volume of the unit cell. Upon charge immediately following the discharge step, the a axis increases, whereas the b and c axes decrease. The variation of the lattice parameters and cell volume can be physically explained by the fact that, upon intercalation, the Mg^{2+} ions pull the V_3O_8 layers, which are stacked along the a axis, closer to each other due to the high charge/size ratio of the cation; simultaneously this results in an expansion of the intralayer atomic rearrangement to accommodate the crystal structure changes associated with intercalation of the Mg^{2+} ion.

Additionally, this trend can also be quantitatively analyzed by considering the percentage change in lattice parameters and cell volume with respect to the previous electrochemical step (Figure S12, Table S2), e.g., comparison of HVO-1D with HVO-OCV or comparison of HVO-50C with HVO-50D. At each discharge, Δa is negative, whereas Δb , Δc and ΔV have positive values. The opposite trend happens during charge.

Previous reports^[29] show that the crystal water, being covalently bonded to the vanadium polyhedral, is not extracted from the structure during electrochemical cycling at 60 °C. Since in our study HVO was tested at ambient temperature, the extraction of water during cycling is not expected. Therefore, the observed structural changes are related to Mg^{2+} (de)intercalation from the HVO structure.

XPS analysis was carried out to study the chemistry of the electrode/electrolyte interface and gain insights into the oxidation state of vanadium and the Mg content during cycling. Figure 4a shows the C1s spectra and Figure 4b shows the O1s and V2p XPS spectra.

The C1s spectra of the pristine sample shows the characteristic peaks of C–C/C–H (284.3 eV), C–O (285.8 eV), and C=O (287.9 eV) bonds related to the conductive carbon present in the electrode as well as the C–F (290.3 eV) peak related to the PVDF binder.^[47] Once the sample is in contact with the electrolyte for 6 h (HVO-OCV), a small peak appears at 292.6 eV related to C–F₃ bond of the TFSI⁻ anion.^[48,49] These findings indicate that already at OCV, a surface layer containing TFSI⁻ anions is present on the surface of HVO. The peaks observed for the HVO-OCV samples are also observed and comparable for all cycled samples.

The O1s spectra of the pristine electrode shows two main contributions. The M–O bond of the metal oxide at 530 eV is attributed to the V–O bonds in the VO₅ polyhedrons, and a very broad peak centered at 531.7 eV to the C–O/C=O groups.^[50] In addition, a peak associated with the S=O group and attributed to the TFSI anion, is reported to occur around

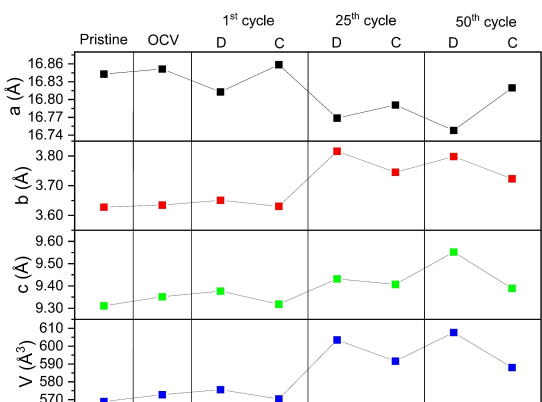


Figure 3. Evolution of HVO lattice parameters (a , b , c) and cell volume at specific cycle numbers.

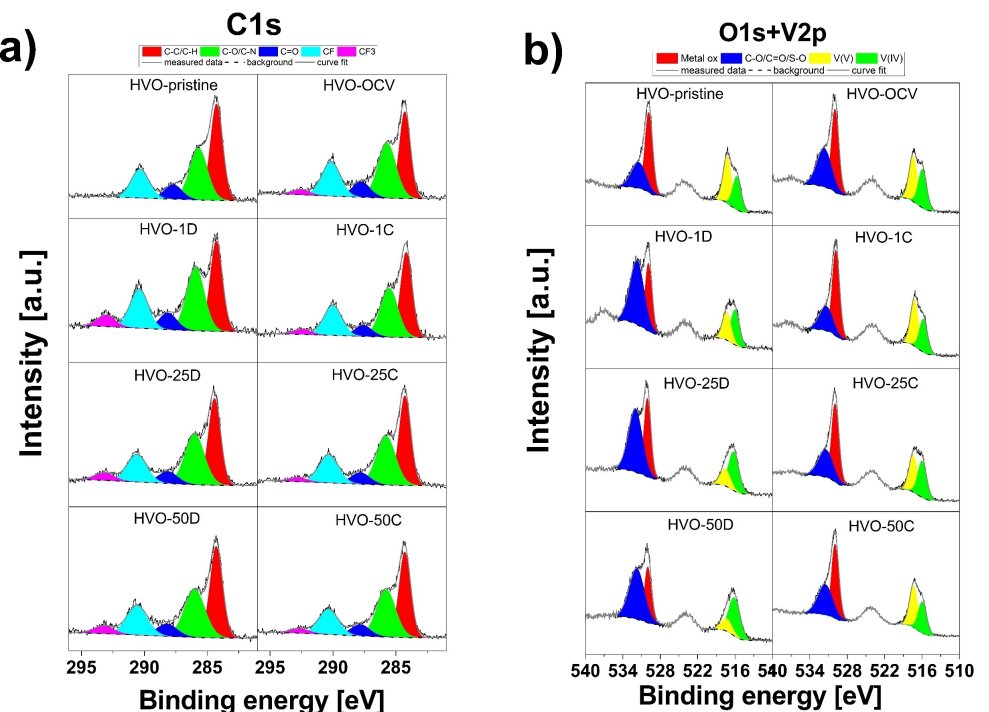


Figure 4. a) C1s and b) O1s and V2p XPS spectra of HVO electrodes

532.7–533 eV.^[49,51] This latter peak increases in intensity for the HVO-OCV sample, indicating that a surface layer is already present on HVO after 6 h at OCV, in agreement with the C1s spectra (Figure 4a). A trend is observed for the cycled samples: the intensity of the S=O peak increases during discharge and decreases upon charge. This is a clear indication that during cycling a surface layer, i.e., a cathode electrolyte interphase (CEI) is formed which contains TFSI⁻ anions. In addition, the thickness of this layer might vary upon cycling, being thicker on discharge than on charge.

The V2p spectra give information about the vanadium oxidation state. As for the pristine sample, V⁵⁺ and V⁴⁺ peaks at 517.3 eV and 515.8 eV,^[52] respectively, are observed as expected due to the mixed oxidation state of vanadium in HVO.^[22] The V⁴⁺ peak slightly increases for the HVO-OCV sample, changing the V⁵⁺/V⁴⁺ ratio from 1.42 for the pristine electrode to 1.17 for the OCV electrode (Table S3). The lower ratio indicates a minimal reduction in the oxidation state of the vanadium ions at the surface during OCV, which can be related to the self-discharge behavior and the intercalation of Mg²⁺ ions into the top surface layers of HVO. Upon discharge, the intercalation of Mg²⁺ into the HVO structure leads to the reduction of vanadium atoms from V⁵⁺ to V⁴⁺ supported by an intensity increase of V⁴⁺ peak and consequently a decrease of the V⁵⁺/V⁴⁺ ratio. Upon charge, the deintercalation of Mg²⁺ ions results in the oxidation of V atoms leading to an increase in intensity and area of the V⁵⁺ peak. The change in oxidation state of V atoms upon cycling confirms the reversibility of the Mg²⁺ de-intercalation into HVO. The evolution of the V⁵⁺/V⁴⁺ ratio is reported in Figure S13. Due to the much higher specific discharge capacities at cycle number 25 and 50 (i.e., higher

amount of Mg²⁺ ions intercalated and consequently a higher amount of V reduced to V⁴⁺), the ratio is lower than for the 1st discharge. Moreover, the V⁵⁺/V⁴⁺ ratio for HVO-25C and HVO-50C does not return to its original value (1.42 for HVO-pristine). This observation fits well with the XRD data after Le Bail fitting where the lattice parameters do not go back to their pristine values (i.e., *a*-parameters for HVO-25C and HVO-50C are lower, whereas the *b* and *c*-parameters are higher)

Surprisingly, the evolution of the surface V⁵⁺/V⁴⁺ ratio extracted from XPS data nearly overlaps with the evolution of the *a* lattice parameter obtained from the fitted XRD data (Figure S13). Therefore, this confirms that the intercalation and trapping of Mg²⁺ ions are controlled by reaction phenomena which occur at both bulk and outer surface levels.

The F1s and Mg1s XPS spectra shown in Figure 5 allow us to gain additional insights about the chemical composition of the CEI on HVO.

The F1s XPS spectra of the HVO-pristine electrode features only one main peak at 687.5 eV for the C–F group related to the PVDF binder.^[47] An additional contribution at 688.6 eV assigned to C–F₃ bond^[48,49] is detected for the HVO-OCV electrode, in agreement with the C1s and O1s confirming the presence of a surface layer at OCV containing TFSI⁻ anions.

Although the C–F₃ contribution is present in all cycled electrodes, the discharged samples show a much higher peak in comparison to the charged samples. A logical explanation seems to be that the CEI layer on the HVO surface is thicker after discharge, and its thickness decreases upon charge, which is most likely due to the generation of components that are soluble in the electrolyte. This agrees with the findings of the O1s spectra described above. Furthermore, an additional

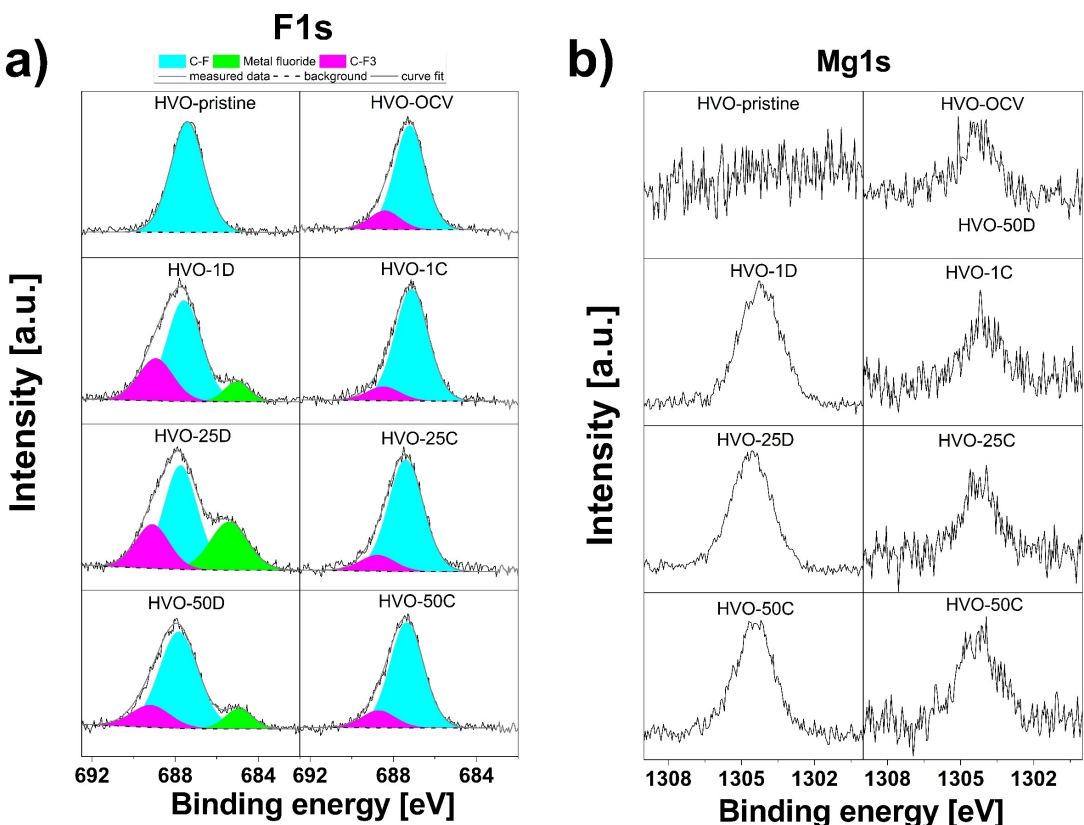


Figure 5. a) F1s and b) Mg1s XPS spectra of HVO electrodes

contribution at 685.0 eV is present for the discharged electrodes. Such a low binding energy in the F1s XPS spectrum is usually related to the M–F (metal-fluoride) bond. Literature reports associate this peak to the formation of MgF_2 as a result of TFSI decomposition.^[49,53,54] The presence of MgF_2 at the end of the discharge indicates that an irreversible reaction is occurring on HVO surface, which might account for the difference in specific capacity between charge and discharge. However, the MgF_2 peak disappears upon charge. Our hypothesis for the disappearance of the MgF_2 peak is related to the change in thickness of the CEI upon cycling. During discharge, the CEI is thicker, contains $TFSI^-$ anions as well as dispersed MgF_2 nanocrystals (from TFSI decomposition). Upon charge, the CEI thickness decreases due to the oxidation reactions, which result in the generation of TFSI components which are soluble into the electrolyte, and the MgF_2 nanocrystals are dispersed into solution and are not visible anymore upon charge. However, our hypothesis requires further investigations and will be the subject of a future publication.

The Mg1s spectra show no peak for the HVO-pristine electrode. However, a small peak is present for the HVO-OCV at around 1304.3 eV, indicating that small amounts of Mg are present on the surface of HVO after 6 h at OCV, in agreement with the self-discharge and the previously analyzed XPS spectra. For example, as reported earlier, the V^{4+} peak slightly increases for the HVO-OCV sample, changing the V^{5+}/V^{4+} ratio from an initial value of 1.42 to 1.17 for the OCV electrode (Table S3), which would be necessary to maintain charge

neutrality during the incorporation of Mg. Discharged samples show a well distinguished peak at 1304.3 eV while charged samples show a much smaller peak centered at the same binding energy due to the lower amount on the HVO surface. However, it is important to note that Mg was detected in all charged samples, demonstrating that Mg^{2+} ions are still present on the surface of HVO upon charge probably due to trapping.

Analysis of the oxidation state of Mg has been performed in a Wagner plot using the BE position of the Mg 1s and kinetic energy (KE) positions of Mg KLL Auger peaks (Figure S14), comparing the results to other known materials. Only small differences are found for different numbers of cycles, while a distinct difference is visible for charging (Auger parameter: 2486 eV) and discharging samples (2484 eV). Furthermore, MgF_2 is the compound having the closest Auger parameters to the discharged samples, giving further support that MgF_2 might be the main compound forming on the HVO surface upon discharge, as supported also by F1s XPS spectra.

The quantification of the Mg content on the HVO surface from the XPS measurements is summarized in Table S3. About 1 at.% was detected for HVO-OCV, and around 5 at.% for the discharged samples. The amount of Mg on the surface of the charged samples increases with the cycle numbers from 0.1 at.% for HVO-1C to 0.8 at.% and 1.7 at.% for HVO-25C and HVO-50C, respectively. This agrees with the qualitative analysis carried out above on Mg1s spectra further confirming the Mg trapping at the HVO surface.

The S2p spectra in Figure S15 shows the presence of S in all electrodes but the pristine. The peak centered at 169.5 eV can be assigned to O=S=O of TFSI⁻ anion, however the broad peak width and the asymmetry at lower binding energies indicate the presence of TFSI decomposition products.^[49,53,55]

SEM micrographs were acquired to investigate the morphology of HVO upon cycling (Figure 6). The pristine HVO electrode is composed of HVO nanorods with a width of 70–120 nm and a length of >1 μm. Due to electrode processing and/or van-der-Waals attractive forces, the nanorods seem to interconnect to form bundles. The conductive carbon (round-

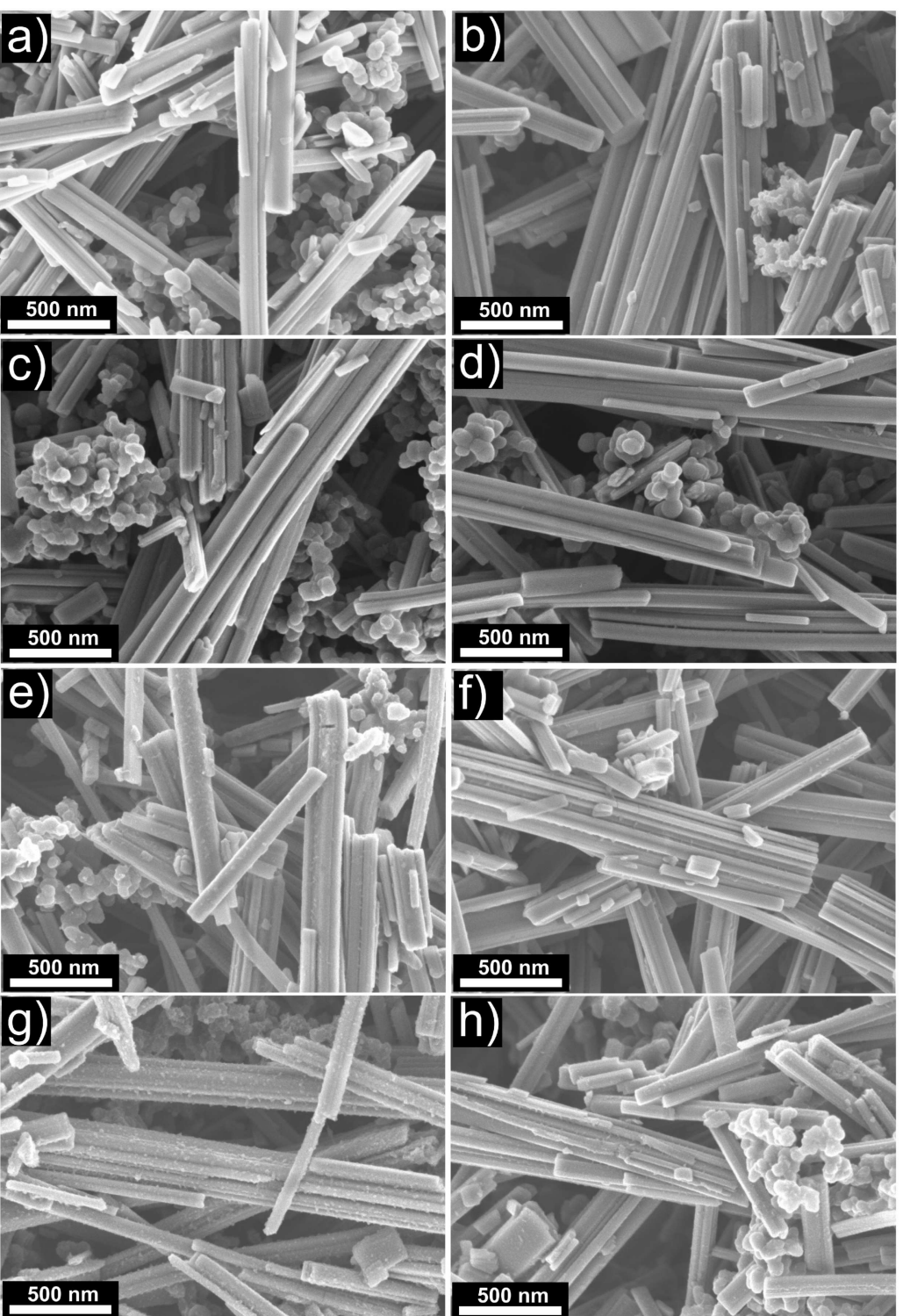


Figure 6. SEM micrographs of the HVO electrodes. a) HVO-pristine, b) HVO-OCV, c) HVO-1D, d) HVO-1C, e) HVO-25D, f) HVO-25C, g) HVO-50D, and h) HVO-50C

shaped nanoparticles) is well distributed in the electrode and interconnects between the HVO bundles, providing pathways for electronic transport. The microstructure of the HVO-OCV electrode shows no difference compared to the pristine electrode. Even though a surface layer was detected by XPS, its thickness is too thin to be detected by electron microscopy. HVO-1D and HVO-1C also do not show any appreciable differences compared to the pristine electrode. However, a surface roughness is visible for the HVO-25D electrode. Even though the width of the nanorods does not seem to change upon discharge, they seem to be covered with a layer of, possibly, electrolyte decomposition products. Such a surface layer seems to be less rough for HVO-25C, indicating that some CEI components, such as MgF_2 , may be lost upon charge, as shown by the XPS evaluation. The surface layer seems to build up over cycling and almost uniformly covers the nanorods in the HVO-50D electrode. The surface layer on the nanorods of the HVO-50C electrode is less rough compared of that for HVO-50D electrode. This effect was also observed for the HVO-25 electrodes and is probably due to a certain extent of dissolution of the surface layer during charge. The integrity and the shape of the nanorods do not seem to change upon cycling or be affected by the charge state.

EDX analysis was carried out on all samples to quantify the amount of Mg present in the samples and correlate these findings with the electrochemistry. The amount of Mg in HVO-OCV and HVO-1C was too little to ensure a reliable quantification. The Mg and V amounts detected for the remaining samples are listed in Table S4. However, rather than the absolute values, the Mg/V ratio is more useful for comparing the EDX and electrochemical data. The Mg/V ratio was calculated from the EDX data, as well as from the electrochemical data (i.e., specific capacity) by considering the number of moles of Mg inserted at each discharge step. The Mg/V ratio from the EDX measurement of HVO-1D is in very good agreement with the Mg/V ratio determined from the cycling data (0.08 and 0.07, respectively). However, HVO-25D and HVO-50D show an EDX Mg/V ratio of 0.21 and 0.25, respectively, which are significantly lower than the Mg/V ratio calculated from the cycling data (0.38 and 0.31, respectively). However, based on the XPS and SEM results presented above, part of the specific capacity during discharge is most probably the result of irreversible reactions occurring at the electrode/electrolyte interphase. Therefore, considering instead that the reversible specific capacity during discharge is close or equal to the specific capacity during charge (i.e., the amount of Mg intercalated into HVO during discharge is as much as that which can be extracted during the successive charge step). According to this evaluation, the reversible capacity of HVO is around 130 mAh g^{-1} , which corresponds to a Mg/V ratio of about 0.23. This value is in agreement with the Mg/V EDX ratio of HVO-25D and HVO-50D. Around 5–6 at.% of Mg was detected by EDX for the HVO-25C and HVO-50C samples due to partial Mg trapping in HVO, which is in good correlation with the XRD and XPS results shown above.

EDX analysis shed some light on the specific capacity fading. Vanadate cathodes suffer from vanadium dissolution in

organic electrolytes^[56] with a higher solubility observed for vanadium ions in a high oxidation state such as V^{5+} and V^{4+} .^[57] EDX of the activated carbon counter electrode after 25 and 50 cycles revealed the presence of vanadium only after 50 cycles (Figure S16). Such a finding can be attributed to the dissolution of V atoms from the HVO structure into the electrolyte. Due to the loss of active material, a slight decrease in specific capacity occurs between 25 and 50 cycles.

Raman spectra were acquired for the pristine sample as well as for the cycled samples to study the changes in the environment around the vanadium atoms upon Mg^{2+} intercalation (Figure 7). The Raman spectra of HVO-pristine shows a main peak at 138 cm^{-1} (peak 1) and two small features at 157 cm^{-1} and 192 cm^{-1} . These low frequency Raman peaks correspond to the lattice vibrations which are strongly associated with the layered structure.^[27,58] The two peaks at 279 (peak 2) and 402 cm^{-1} (peak 3) are assigned to the bending vibrations of the V–O bonds.^[58] The spectrum of the HVO electrodes maintained at OCV for 6 hours shows minor changes. A shoulder appears at 118 cm^{-1} and peak 2 shifts only slightly to lower wavenumbers (267 cm^{-1}). However, major changes are observed for HVO-1D electrodes. The intensity of the main peak at 138 cm^{-1} decreases, a new peak appears at 118 cm^{-1} (peak 4) and peak 2 shifts to lower wavenumbers (261 cm^{-1}). Since these peaks are correlated to the layered structure, it is expected that these changes in the spectra result from the presence of Mg in the HVO structure. Specifically, the peak at around 118 cm^{-1} was already observed for the intercalation of divalent ions, i.e., Zn^{2+} into HVO^[27] and the shift of peak 2 to lower wavenumbers can be correlated to the

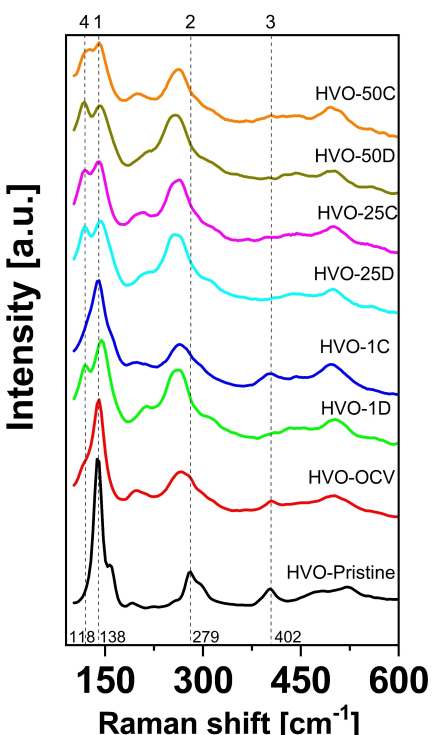


Figure 7. Raman spectra of HVO electrodes

longer V–O bond length upon intercalation.^[29] Upon 1st charge, peak 4 decreases in intensity and remains mainly as a shoulder on the main peak, and peak 2 shifts slightly back to higher wavenumbers (264 cm^{-1}). The Raman spectra of HVO-25D shows a much stronger appearance of peak 4, associated with the intercalation of Mg^{2+} ions; however, upon 25th charge the peak is still present, indicating only partial extraction of Mg ions from HVO structure supporting the hypothesis shown above by XRD and XPS on Mg trapping. Similar conclusions as for the 25th cycle, can be drawn for the 50th cycle.

The in-depth characterization carried out on pristine and cycled electrodes allows us to describe in detail the structural, morphological and interfacial modifications HVO undergoes upon electrochemical magnesiation in TFSI-based electrolytes (Figure 8).

HVO undergoes self-discharge while in contact with the electrolyte at OCV for 6 h. As a result, nominal amounts of Mg^{2+} ions are intercalated into HVO as shown by the change in XPS $\text{V}^{5+}/\text{V}^{4+}$ ratio and the slight shift in peak 2 of the Raman spectra. The driving force for the self-discharge might be the instability of the highly oxidizing V^{5+} ions when placed in contact with the electrolyte. Therefore, Mg^{2+} ions spontaneously intercalate into a few atomic layers on the surface of HVO and more stable V^{4+} ions are formed. This intercalation only slightly affects the bulk crystal structure with very minor changes in the cell volume. Instead, the formation of a surface layer can be already observed at OCV probably, as a result of the adsorption of TFSI^- anions on HVO surface (Figure 8b).

Based on the measured capacity of $\approx 40\text{ mAh g}^{-1}$ upon 1st discharge, around 0.2 equiv. of Mg are expected to be intercalated into HVO. The intercalation of Mg^{2+} ions changes the lattice parameters and volume of the unit cell slightly more than for the OCV samples. XPS and Raman spectra both confirm the intercalation of Mg^{2+} with a change in $\text{V}^{5+}/\text{V}^{4+}$ ratio and the appearance of a new Raman peak at low frequencies (peak 4). EDX also further confirms the Mg/V ratio extracted from cycling data on discharge. The appearance of a metal-fluoride peak in the XPS supports the hypothesis of a MgF_2 -containing CEI. TFSI anions and its decomposition products are present on the surface of HVO (Figure 8c).

Upon 1st charge the unit cell parameters, XPS $\text{V}^{5+}/\text{V}^{4+}$ ratio and Raman peak positions return close to their original values for the pristine electrode, but never quite attain their original values. This indicates a reversible deintercalation process, although some Mg is still present into HVO structure after 1st charge. The decreased intensities of the S=O and CF_3 peaks and the disappearance of MgF_2 peak in the XPS data on the 1st charge indicated that the CEI is mainly TFSI-based and probably decreases in thickness upon charge. No important morphological changes are observed up to this point (Figure 8d).

Upon the 25th discharge, the intercalation of a higher amount of Mg^{2+} ions considerably affects the unit cell axes and volume, with a decrease in the a parameter and an increase in the b , and c parameters as well as in the volume, the latter increases by 6%. The intercalation is further supported by a lower XPS $\text{V}^{5+}/\text{V}^{4+}$ ratio and the appearance of Raman peaks at

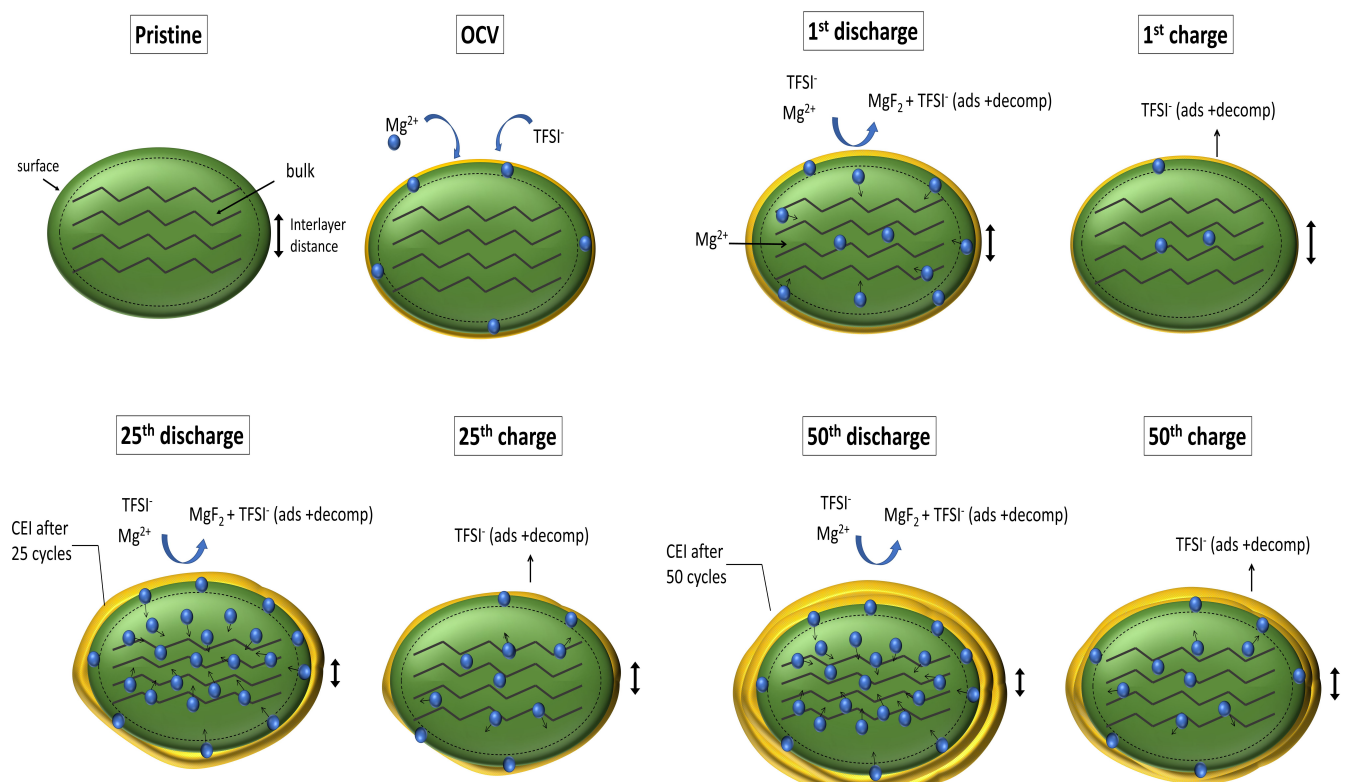


Figure 8. Summary of the modifications occurring in HVO during cycling.

low frequencies. By using the Mg/V ratio calculated by EDX analysis, around 0.7 equiv. of Mg^{2+} ions are intercalated into the HVO crystal structure. However, higher values are extracted from cycling data, (i.e., 1.15). This additional capacity is most probably the result of electrolyte decomposition and formation of a CEI on the HVO surfaces. Indeed, not only XPS analysis supports the presence of a CEI containing MgF_2 and TFSI, but also a distinct surface roughening could be observed in the SEM micrographs. Therefore, a much thicker CEI can be expected in comparison to the 1st discharge (Figure 8e). Upon 25th charge, the unit cell parameters change in the opposite direction (i.e., a increases and b, c and volume decreases) and the XPS V^{5+}/V^{4+} ratio increases. However, the values do not return to those measured for the pristine electrode. Also, the Raman spectra of the 25th charged sample is very similar to the 25th discharged sample. Therefore, it is expected that a certain amount of Mg is trapped in the HVO structure and cannot be extracted upon charge. In addition, the intercalation of Mg^{2+} causes irreversible changes to the crystal structure. As shown for the 1st charge, the CEI layer after the 25th charge contains mainly TFSI anions and its decomposition products, since MgF_2 was not detected by XPS, and a decrease in surface roughness can be observed in the SEM micrographs (Figure 8f).

Due to the considerable changes in the lattice parameters between cycle 1 and cycle 25, a gradual structural deformation to accommodate Mg^{2+} ions is the most probable cause for the increase in specific capacity in the initial cycles. In addition, the increase in specific capacity causes a higher number of ions to go through the electrode/electrolyte interface, resulting in a more extensive TFSI decomposition into MgF_2 . At the same time, because of the high capacity, an increasingly larger amount of Mg ions are trapped in HVO. These two phenomena give rise to the increase in irreversible discharge specific capacity up to cycle 25 (i.e., increase in gap between charge and discharge).

After 50 cycles (Figure 8g and h), the discharged and charged electrodes follow the trends already shows for the electrodes after 25th cycles. The CEI layer is much thicker and visible after 50th discharge, as shown by the increased roughness on HVO nanowires and vanadium dissolution detected by EDX which accounts for the slow capacity fading.

Conclusion

A detailed study of the changes occurring in HVO cathode material upon cycling in $Mg(TFSI)_2$ -based electrolytes revealed that the layered crystal structure, the surface morphology as well as the chemistry of the electrode-electrolyte interphase are strongly affected by Mg^{2+} intercalation. The extent of the changes varies depending on the charge state and cycle number. Structural characterization showed minor changes during the 1st cycle but a shortening of the interlayer distance upon intercalation and a considerable increase in unit cell volume during discharge for prolonged cycling. The change in unit cell parameters and volume is reversed during charge but the values do not return to those for the pristine electrode due

to Mg trapping in the HVO structure. Surface chemical analysis showed that the CEI has a different chemical composition and thickness depending on the charge state and cycle number. Upon discharge the CEI is thicker, appearing as surface roughness in the SEM micrographs of the HVO nanowires. This layer is mainly composed of organic components, i.e., TFSI and its decomposition products, as well as inorganic components, i.e., MgF_2 . Upon charge its thickness decreases and it is mainly organic-based. Reversible changes in the oxidation states of the vanadium ions were observed upon cycling, and the V^{5+}/V^{4+} ratio from the surface XPS analysis is in perfect agreement with the change in the a lattice parameter of the bulk phase, confirming that the changes affect both surface and bulk of HVO. Bulk chemical analysis showed evidence of Mg still being present in HVO upon charge, i.e., the occurrence of Mg trapping. By comparison between the Mg/V ratio extracted from the electrochemical data and from chemical analysis, together with the above-described findings, it was possible to confirm that the additional capacity during discharge is most probably related to irreversible reactions involving the decomposition of the electrolyte on the surface of HVO. In addition, the slow capacity fading occurring between cycle 25 and cycle 50 was associated to V dissolution into the electrolyte.

The results of our study provide a deeper analysis on how Mg^{2+} intercalation affects the structure and surface chemistry of HVO, and its interaction with TFSI-based electrolytes upon cycling. Understanding the changes cathode materials undergo upon cycling and insertion of multivalent guest ions, as well as their reactivity with not-yet commercial electrolytes is of crucial importance for enabling the rational design of next generation cathodes for high energy post-lithium batteries.

Experimental Section

Synthesis of $H_2V_3O_8$

HVO was synthesized by the hydrothermal route using V_2O_5 as a precursor. In a typical synthesis, 2 g of V_2O_5 (Sigma Aldrich) were dispersed in 20 mL of ultra-pure water (MilliQ 18.2 MΩ) in a round-bottom flask. Successively, 0.09 g of ascorbic acid (Sigma Aldrich) were added to the suspension, which was stirred under reflux at 110 °C for 3 h. After this step, the green suspension was transferred into a 50 mL PTFE vessel of an autoclave. The autoclave was sealed, and the suspension was treated hydrothermally for 4 h at 160 °C and then for 10 h at 220 °C. At the end of the reaction, the green solid was filtered, washed with ultra-pure water and dried overnight at 80 °C in a vacuum oven.

Electrode preparation and electrochemical cycling

The as-synthesized $H_2V_3O_8$ powder was used for electrode preparation. The slurries were prepared using 80 wt.% of $H_2V_3O_8$ as the active material, 10 wt.% of C-NERGY SuperC45 (average particle size = 37 nm, $S_{BET} = 45 \text{ m}^2 \text{ g}^{-1}$) as the conductive additive, 10 wt.% of PVDF 5120 (Solef® PVDF, Solvay SA) as the binder, and N-methyl-2-pyrrolidone (NMP, Sigma-Aldrich, 99%) as solvent. The binder was pre-dissolved in NMP to form an 8 wt.% solution. In a standard preparation, SuperC45 carbon was added into the appropriate amount of binder solution and stirred for about 10 min. Success-

sively, HVO was added to the solution together with small amounts of NMP solvent to adjust the viscosity of the slurry. The solution was left to stir overnight using a magnetic stirrer. The resulting, homogenized slurry was casted onto aluminum foil (15 µm thickness, MTI corporation) using the doctor-blade technique with a blade gap of 60 µm. The casted electrode sheets were dried under vacuum at 80 °C overnight. Circular electrodes of 15 mm-diameter were punched out and re-dried overnight at 120 °C using a Büchi® glass oven to remove any remaining traces of water before being introduced into an Ar filled glove box (<0.1 ppm H₂O and <0.1 ppm O₂). The electrode loading was around 1–1.5 mg cm⁻².

ECC-Std cells (EL-cell) were assembled using the as-prepared electrodes as working electrodes, activated carbon (AC, Kynol ACC-5092-20 carbon cloth, specific surface area: 1800 m² g⁻¹) as the counter and quasi-reference electrode, a glass fiber separator (Whatman, GF/C) and 400 µL of electrolyte solution. The mass of the AC was around 14 mg cm⁻², which is approximately 14 times the mass of the active material. Prior to use, the AC was dried overnight at 120 °C under vacuum. The potential of the AC was calibrated with the ferrocene/ferrocenium redox couple, and it was estimated to be 2.55 V vs. Mg²⁺/Mg (rounded for clarity to 2.6 V vs. Mg²⁺/Mg) (Figure S17). The electrolyte used in this study was 0.1 M Mg(TFSI)₂ in acetonitrile (ACN, 99.8%, anhydrous). Prior to the electrolyte solution preparation, Mg(TFSI)₂ (99.5%, Solvionic) was dried under vacuum at 170 °C overnight and ACN was dried on molecular sieves (4 Å) for 72 h inside an Ar-filled glovebox. The electrolyte solution was then prepared by stirring the appropriate amount of Mg salt into ACN overnight. The water-content of the electrolyte was determined to be 40 ppm by Karl-Fisher titrator. Electrochemical measurements were carried out using a BioLogic MPG-2 potentiostat at ambient temperature. Galvanostatic cycling was performed at 10 mA g⁻¹ between -1.5 V and 1.0 V vs. AC. Cyclic voltammetry was performed at 0.1 mV s⁻¹ between -1.5 V and 1.0 V vs. AC.

The pristine electrodes (not cycled) were stored in the glove box after preparation and analyzed as is. The sample preparation for post-mortem characterization techniques was carried out as follows: OCV electrodes – the cells were assembled and maintained at OCV for 6 h; cycled electrodes – the cells were cycled in galvanostatic mode for 1, 25 or 50 cycles, starting with a discharge (magnesiation) step. Once the cycling reached the desired cycle number, cells were stopped either in the charged (1.0 V vs. AC, 3.6 V vs. Mg²⁺/Mg) or discharged states (-1.5 V vs. AC, 1.1 V vs. Mg²⁺/Mg). In all cases, the cells were quickly transferred into the glove box to avoid any relaxation and were disassembled to collect the electrodes. The electrodes were washed several times with anhydrous ACN and allowed to dry inside the glovebox. These cycled electrodes were subjected to further analysis as described below. The analyzed electrodes are named throughout the text as described in Table 1.

Post-mortem characterization of electrodes

Powder X-ray diffraction (XRD) measurements were performed on all samples using a XPert Pro diffractometer (Malvern/Panalytical) equipped with Cu-K_α radiation ($\lambda = 1.54060 \text{ \AA}$) and an X'Celerator linear detector operating in Bragg-Brentano geometry ($\theta/2\theta$). The diffraction patterns were recorded between 10° and 120° (2θ) with an angular step interval of 0.033°. The electrodes for the XRD measurements were sealed inside an air-tight, polycarbonate dome in an Ar-filled glovebox to prevent exposure to ambient air during the XRD measurements.

Unit cell parameters were refined by Le Bail fitting using the GSAS suite of programme.^[59,60] The models used for the refinements were

based on the published structures of HVO and MgHVO^[29] for the charged and discharged electrodes, respectively.

Sample morphologies were investigated by scanning electron microscopy (SEM) using a Carl Zeiss Supra 40 scanning electron microscope with Everhart-Thornley (ETD) and Through-Lens (TLD) detectors with a primary electron-beam energy of 2 keV. The elemental distribution was analyzed by energy dispersive X-ray spectroscopy (EDS) using an Octane Elect detector (EDX, EDAX Inc., Mahwah, NJ, USA) and an electron-beam energy of 20 keV. Electrodes were fixed onto a SEM sample holder in the glovebox and transferred to the SEM in an air-tight vessel. The maximum contact time of the electrodes with air during transfer to the SEM chamber was 3–5 seconds on average.

XPS measurements were carried out on a SPECS XP-spectrometer equipped with a monochromatic Al-K_α X-ray source (μ Focus 350) and a hemispherical WAL-150 analyzer (acceptance angle: 60°). Pass energies of 100 and 30 eV and step widths of 0.5 eV and 50 meV were used for the survey and detail spectra respectively (excitation energy: 1486.6 eV, beam energy and spot size: 100 W onto 500 µm; mean angle: 51° to sample surface normal; base pressure: $4 \times 10^{-10} \text{ mbar}$, pressure during measurements: $1 \times 10^{-9} \text{ mbar}$). Linearity of the binding energy (BE) scale was confirmed by using methods described in ISO15472. The samples were stored in an Ar filled glove box before and after the XPS measurements (maximum air exposure time 20–30 s for inserting and removing from the ultra-high vacuum system). All samples were fixed on the holder using Ta clips. Data analysis was performed using CASA XPS software, employing transmission corrections, Shirley/Tougaard backgrounds and Scofield sensitivity factors. No charge correction was applied (C1s signal is around 284.5–284.8 eV). Deconvolution of spectra was carried out using Gaussian-Lorentzian peaks (GL(30)).

The Raman spectra were recorded at room temperature using a Xplora Plus Raman confocal microscope (Jobin-Yvon-Horiba) equipped for signal detection with a highly sensitive CCD-detector with thermoelectric cooling down to -60 °C. A Nd:YAG laser (532 nm) was used as the excitation source. The laser was focused onto the sample using a 50× magnifying objective. Spectra were recorded in air with a 1200 gr/mm grating, using an acquisition time of 30 s and an accumulation number of 5.

Supporting Information

Supporting information are provided in a separate file.

Acknowledgements

This work was partially funded by the Austrian Federal Ministry for Climate Action, Environment, Energy, Mobility, Innovation and Technology. Dr. Nicolas Eshraghi is gratefully acknowledged for supporting the paper with his artistic touch.

Conflict of Interest

The authors declare no conflict of interest.

Data Availability Statement

The data that support the findings of this study are available from the corresponding author upon reasonable request.

Keywords: cathode · electrolyte · interphase · $H_2V_3O_8$ · intercalation · magnesium-ion batteries · vanadates

- [1] I. Tsioropoulos, D. Tarvydas, N. Lebedeva, *Publ. Off. Eur. Union* **2018**, 1–72.
- [2] Z. Guo, J. Zhu, J. Feng, S. Du, *RSC Adv.* **2015**, 5, 69514–69521.
- [3] M. Keersemaker, *Critical Raw Materials. In: Suriname Revisited: Economic Potential of its Mineral Resources. SpringerBriefs in Earth Sciences*, Springer, Cham, **2020**, pp. 69–82.
- [4] S. S. Sharma, A. Manthiram, *Energy Environ. Sci.* **2020**, 13, 4087–4097.
- [5] Y. Tian, G. Zeng, A. Rutt, T. Shi, H. Kim, J. Wang, J. Koettgen, Y. Sun, B. Ouyang, T. Chen, Z. Lun, Z. Rong, K. Persson, G. Ceder, *Chem. Rev.* **2021**, 121, 1623–1669.
- [6] J. W. Choi, D. Aurbach, *Nat. Rev. Mater.* **2016**, 1, 16013.
- [7] F. Maroni, S. Dongmo, C. Gauckler, M. Marinaro, M. Wohlfahrt-Mehrens, *Batteries & Supercaps* **2021**, 4, 1221–1251.
- [8] Y. Gao, Z. Pan, J. Sun, Z. Liu, J. Wang, *High-Energy Batteries: Beyond Lithium-Ion and Their Long Road to Commercialisation*, Springer Singapore, **2022**.
- [9] C. Kuang, W. Zeng, Y. Li, *J. Nanosci. Nanotechnol.* **2019**, 19, 12–25.
- [10] F. W. Clarke, *The Data of Geochemistry*, Washington, D. C., **1924**.
- [11] H. Tang, Z. Peng, L. Wu, F. Xiong, C. Pei, Q. An, L. Mai, *Electrochem. Energy Rev.* **2018**, 1, 169–199.
- [12] C. Ling, D. Banerjee, M. Matsui, *Electrochim. Acta* **2012**, 76, 270–274.
- [13] M. Matsui, *J. Power Sources* **2011**, 196, 7048–7055.
- [14] E. Levi, Y. Gofer, D. Aurbach, *Chem. Mater.* **2010**, 22, 860–868.
- [15] M. M. Huie, D. C. Bock, E. S. Takeuchi, A. C. Marschilok, K. J. Takeuchi, *Coord. Chem. Rev.* **2015**, 287, 15–27.
- [16] M. Mao, T. Gao, S. Hou, C. Wang, *Chem. Soc. Rev.* **2018**, 47, 8804–8841.
- [17] Z. Ma, D. R. MacFarlane, M. Kar, *Batteries & Supercaps* **2019**, 2, 115–127.
- [18] Z. Li, L. Han, Y. Wang, X. Li, J. Lu, X. Hu, *Small* **2019**, 15, 1–16.
- [19] X. Zhang, X. Sun, X. Li, X. Hu, S. Cai, C. Zheng, *J. Energy Chem.* **2021**, 59, 343–363.
- [20] Y. Yue, H. Liang, *Adv. Energy Mater.* **2017**, 7, 1–32.
- [21] M. Clites, B. W. Byles, E. Pomerantseva, *Adv. Mater. Lett.* **2017**, 8, 679–688.
- [22] M. Simões, Y. Mettan, S. Pokrant, A. Weidenkaff, *J. Phys. Chem. C* **2014**, 118, 14169–14176.
- [23] J. Prado-Gonal, B. Molero-Sánchez, D. Ávila-Brande, E. Morán, J. C. Pérez-Flores, A. Kuhn, F. García-Alvarado, *J. Power Sources* **2013**, 232, 173–180.
- [24] D. Söllinger, M. Karl, G. J. Redhammer, J. Schoiber, V. Werner, G. A. Zickler, S. Pokrant, *ChemSusChem* **2021**, 14, 1112–1121.
- [25] D. Wang, Q. Wei, J. Sheng, P. Hu, M. Yan, R. Sun, X. Xu, Q. An, L. Mai, *Phys. Chem. Chem. Phys.* **2016**, 18, 12074–12079.
- [26] D. Söllinger, T. Berger, G. J. Redhammer, J. Schoiber, S. Pokrant, *ChemElectroChem* **2021**, 8, 4223–4232.
- [27] P. He, Y. Quan, X. Xu, M. Yan, W. Yang, Q. An, L. He, L. Mai, *Small* **2017**, 13, DOI: 10.1002/smll.201702551.
- [28] H. Tang, N. Xu, C. Pei, F. Xiong, S. Tan, W. Luo, Q. An, L. Mai, *ACS Appl. Mater. Interfaces* **2017**, 9, 28667–28673.
- [29] M. Rastgoo-Deylami, M. S. Chae, S.-T. Hong, *Chem. Mater.* **2018**, 30, 7464–7472.
- [30] F. Theobald, R. Cabala, C. R. Acad. Sc. Paris Ser. C **1970**, 270, 2138.
- [31] Y. Oka, T. Yao, N. Yamamoto, *J. Solid State Chem.* **1990**, 89, 372–377.
- [32] Y. Mettan, R. Caputo, T. Chatterji, *RSC Adv.* **2015**, 5, 106543–106550.
- [33] Q. An, J. Sheng, X. Xu, Q. Wei, Y. Zhu, C. Han, C. Niu, L. Mai, *New J. Chem.* **2014**, 38, 2075–2080.
- [34] N. Sa, H. Wang, D. L. Proffit, A. L. Lipson, B. Key, M. Liu, Z. Feng, T. T. Fister, Y. Ren, C. J. Sun, J. T. Vaughay, P. A. Fenter, K. A. Persson, A. K. Burrell, *J. Power Sources* **2016**, 323, 44–50.
- [35] Z. Lu, A. Schechter, M. Moshkovich, D. Aurbach, *J. Electroanal. Chem.* **1999**, 466, 203–217.
- [36] D. Aurbach, Y. Gofer, Z. Lu, A. Schechter, O. Chusid, H. Gizbar, Y. Cohen, V. Ashkenazi, M. Moshkovich, R. Turgeman, E. Levi, *J. Power Sources* **2001**, 97–98, 28–32.
- [37] D. Söllinger, G. J. Redhammer, J. Schoiber, G. A. Zickler, S. Pokrant, *Electrochim. Acta* **2022**, 434, 141294.
- [38] Q. D. Truong, M. Kempaiah Devaraju, P. D. Tran, Y. Gambe, K. Nayuki, Y. Sasaki, I. Honma, *Chem. Mater.* **2017**, 29, 6245–6251.
- [39] D. Kim, J. H. Ryu, *Electron. Mater. Lett.* **2019**, 15, 415–420.
- [40] Z. Li, X. Mu, Z. Zhao-Karger, T. Diemant, R. J. Behm, C. Kübel, M. Fichtner, *Nat. Commun.* **2018**, 9, 5115.
- [41] Q. An, Y. Li, H. Deog Yoo, S. Chen, Q. Ru, L. Mai, Y. Yao, *Nano Energy* **2015**, 18, 265–272.
- [42] C. Wu, G. Zhao, X. Bao, X. Chen, K. Sun, *J. Alloys Compd.* **2019**, 770, 914–919.
- [43] J. L. Andrews, A. Mukherjee, H. D. Yoo, A. Parija, P. M. Marley, S. Fakra, D. Prendergast, J. Cabana, R. F. Klie, S. Banerjee, *Chem* **2018**, 4, 564–585.
- [44] S. H. Lee, R. A. DiLeo, A. C. Marschilok, K. J. Takeuchi, E. S. Takeuchi, *ECS Electrochem. Lett.* **2014**, 3, A87–A90.
- [45] Y. Zhu, G. Huang, J. Yin, Y. Lei, A. Emwas, X. Yu, O. F. Mohammed, H. N. Alshareef, *Adv. Energy Mater.* **2020**, 10, 2002128.
- [46] Q. Pang, C. Sun, Y. Yu, K. Zhao, Z. Zhang, P. M. Voyles, G. Chen, Y. Wei, X. Wang, *Adv. Energy Mater.* **2018**, 8, 1800144.
- [47] B. Heidrich, M. Börner, M. Winter, P. Niehoff, *J. Energy Storage* **2021**, 44, 103208.
- [48] V. Sharova, A. Moretti, T. Diemant, A. Varzi, R. J. Behm, S. Passerini, *J. Power Sources* **2018**, 375, 43–52.
- [49] T. Gao, S. Hou, K. Huynh, F. Wang, N. Eidson, X. Fan, F. Han, C. Luo, M. Mao, X. Li, C. Wang, *ACS Appl. Mater. Interfaces* **2018**, 10, 14767–14776.
- [50] R. Tatara, P. Karayalali, Y. Yu, Y. Zhang, L. Giordano, F. Maglia, R. Jung, J. P. Schmidt, I. Lund, Y. Shao-Horn, *J. Electrochem. Soc.* **2019**, 166, A5090–A5098.
- [51] A. Foelske-Schmitz, D. Weingarth, R. Kötz, *Surf. Sci.* **2011**, 605, 1979–1985.
- [52] M. C. Biesinger, L. W. M. Lau, A. R. Gerson, R. S. C. Smart, *Appl. Surf. Sci.* **2010**, 257, 887–898.
- [53] R. Jay, A. W. Tomich, J. Zhang, Y. Zhao, A. De Gorostiza, V. Lavallo, J. Guo, *ACS Appl. Mater. Interfaces* **2019**, 11, 11414–11420.
- [54] R. Attias, M. Salama, B. Hirsch, R. Pant, Y. Gofer, D. Aurbach, *ACS Energy Lett.* **2019**, 4, 209–214.
- [55] M. S. Ding, T. Diemant, R. J. Behm, S. Passerini, G. A. Giffin, *J. Electrochem. Soc.* **2018**, 165, A1983–A1990.
- [56] C. Szczuka, R. A. Eichel, J. Granwehr, *ACS Appl. Energ. Mater.* **2022**, 5, 449–460.
- [57] M. A. Cambaz, B. P. Vinayan, S. A. Pervez, R. E. Johnsen, H. Geßwein, A. A. Guda, Y. V. Rusalev, M. K. Kinyanjui, U. Kaiser, M. Fichtner, *Chem. Mater.* **2019**, 31, 7941–7950.
- [58] S. H. Lee, H. M. Cheong, M. J. Seong, P. Liu, C. E. Tracy, A. Mascarenhas, J. R. Pitts, S. K. Deb, *Solid State Ionics* **2003**, 165, 111–116.
- [59] A. C. Larson, R. B. Von Dreele, General Structure Analysis System (GSAS), Los Alamos National Laboratory Report LAUR 86–748, **2004**.
- [60] A. Le Bail, *Powder Diff.* **2005**, 20, 316–326.

Manuscript received: December 21, 2022

Revised manuscript received: January 31, 2023

Accepted manuscript online: February 3, 2023

Version of record online: February 14, 2023